



Electrolubrication in liquid mixtures between two parallel plates

Roni Kroll¹ and Yoav Tsori^{1,†}

¹Department of Chemical Engineering, Ben-Gurion University of the Negev, Rager Street, Beer-Sheva 84105, Israel

(Received 27 August 2023; revised 7 January 2024; accepted 7 February 2024)

We describe theoretically ‘electrolubrication’ in liquid mixtures: the phenomenon whereby an electric field applied transverse to the confining surfaces leads to concentration gradients that alter the flow profile significantly. When the more polar liquid is the less viscous one, the stress in the liquid falls on two electric-field-induced thin lubrication layers. The thickness of the lubrication layer depends on the Debye length and the mixture correlation length. For the simple case of two parallel and infinite plates, we calculate explicitly the liquid velocity profile and integrated flux. The maximum liquid velocity and flux can be increased by a factor α , of order 10–100 or even more. For a binary mixture of water and a cosolvent, with viscosities η_w and η_{cs} , respectively, α increases monotonically with inter-plate potential V and average ion content, and is large if the ratio η_{cs}/η_w is large.

Key words: electrohydrodynamic effects, multiphase flow, microfluidics

1. Introduction

Confinement of liquids by solid surfaces is common in everyday life and in industrial applications. The relative movement between liquids and the surfaces that confine them affects wear and tear, lubrication, and energy consumption (Hu & Granick 1998; Lugt 2009). These occur whether the surfaces move past each other or if the liquids are pumped in pipes or channels by external forcing. The importance of these processes has led to intensive industrial and fundamental research (Klein 1996; Gropper, Wang & Harvey 2016). Control of the lubrication properties of liquids is desirable in many circumstances. For example, switchable drag reduction could provide a method to increase or decrease the flow in channels or pipes (Terwagne, Brojan & Reis 2014). Electrorheological fluids are particle suspensions that respond to the application of an external electric field (Hao 2001). The long-range interactions between the induced dipoles lead to particle chaining and a dramatic increase of the suspension’s viscosity. In the viscoelectric effect, a liquid’s

† Email address for correspondence: tsori@bgu.ac.il

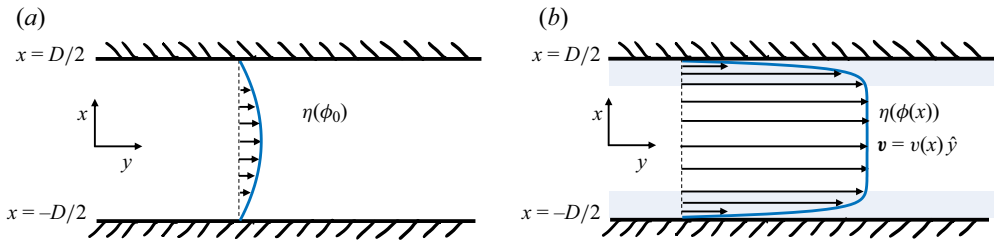


Figure 1. Schematic illustration of the channel. Two flat and smooth walls parallel to y - z plane are separated by a distance D in the x -direction. The confined mixture is flowing along y . In steady state, the velocity depends on x : $\mathbf{v} = v(x)\hat{y}$. (a) When the mixture is homogeneous, its viscosity is $\eta(\phi_0)$ and the flow is the classic parabolic profile. (b) When a potential is applied across the walls, the mixture phase separates and two regions rich in the more polar solvent appear near the walls (faint blue shade). When the more polar solvent is the less viscous one, the lubrication layers modify the flow profile. The strong shear near the surfaces facilitates a large flux.

viscosity changes due the coupling of an electric field with molecular dipoles (Andrade & Dodd 1939, 1946).

Room-temperature ionic liquids attracted considerable interest in recent years as thin-film wear protectors and in energy applications (Marsh, Boxall & Lichtenhaler 2004). The arrangement of the molecules near a charged surface is not trivial due to screening of the field, packing in layers, steric effects, and size asymmetry between anions and cations (Sweeney *et al.* 2012; Bresme *et al.* 2022; Pivnic *et al.* 2023). The effective viscosity of a film can be measured with an atomic force microscope or surface force balance, and usually it increases with the charge of the confining surface (Fajardo *et al.* 2017; Pivnic *et al.* 2020).

Recently, we found a new effect that we call ‘electrolubrication’, whereby the effective viscosity of liquid mixtures can be controlled by electric fields (Tsori 2023). Here, a field transverse to the confining surfaces couples differently to the mixture’s constituents, and screening by existing ions leads to layering of the mixture. The different viscosities of the pure constituents facilitate larger shear, which changes the flow. When the more polar liquid is the less viscous one, lubrication at surfaces is enhanced. In that work, we focused on lubrication between moving surfaces. The unperturbed velocity gradient (without imposed potential) and the resulting stress were constant. The maximal unperturbed velocity was at the moving surface, where the more polar liquid adsorbs. Here, we extend the theory to flows in channels between stationary walls, where the stress is not constant and the maximal unperturbed velocity is where there is less polar liquid. The velocity vanishes at the boundary, where the polar liquid adsorbs.

2. Model

Consider a binary mixture of two liquids. The more polar liquid may be water, and the less polar one is a partially miscible cosolvent. The volume fraction, permittivity and viscosity of the water are ϕ , ϵ_w and η_w , respectively. The same quantities for the cosolvent are denoted by ϕ_{cs} , ϵ_{cs} and η_{cs} . The mixture is coupled to a reservoir containing dissolved anions and cations whose number density is n_0 . The water and cosolvent have partial miscibility given by their coexistence (binodal) curve. It is assumed that the bulk water composition, $\phi = \phi_0$ and temperature correspond to a homogeneous (mixed) state. While the theory is general, in some curves, as an example for a liquid pair, we use the properties of water and glycerol.

The mixture is pumped into a gap between two parallel and smooth surfaces, and flows parallel to the y -direction; see figure 1. The pressure gradient along the gap can result

from a pump, gravitational force, etc. The length of the channel is L , and its walls are at $x = \pm D/2$. An electrostatic potential is applied across the channel in the x -direction. The resultant electric field modifies the mixture's composition and leads to composition gradients perpendicular to the main flow direction. We assume long channels where edge effects can be ignored. The system is then effectively one-dimensional, and all quantities depend on the x -coordinate only. In addition, we focus on steady-state conditions.

We start by formulating the flow behaviour based on a generic mixture free energy density f , and only later choose a specific model. The governing equations for the flow velocity \mathbf{v} , mixture composition ϕ , ion densities n^\pm , and electrostatic potential ψ are (Samin & van Roij 2017)

$$\nabla \cdot \mathbf{v} = 0, \tag{2.1}$$

$$\frac{\partial \phi}{\partial t} + \mathbf{v} \cdot \nabla \phi = \nabla \cdot \left(D_\phi \nabla \frac{\delta f}{\delta \phi} \right), \tag{2.2}$$

$$\rho \left(\frac{\partial \mathbf{v}}{\partial t} + (\mathbf{v} \cdot \nabla) \mathbf{v} \right) = -\nabla p + \nabla \left(\eta \nabla \mathbf{v} + \eta (\nabla \mathbf{v})^\dagger \right) - \phi \nabla \frac{\delta f}{\delta \phi} + \mathbf{f}_{elec}, \tag{2.3}$$

$$\nabla \cdot (\varepsilon_0 \varepsilon \nabla \psi) = e (n^- - n^+), \tag{2.4}$$

$$\frac{\partial n^\pm}{\partial t} + \nabla \cdot (n^\pm \mathbf{v}) = \nabla \cdot \left(D_i \nabla \frac{\delta f}{\delta n^\pm} \right). \tag{2.5}$$

Equation (2.1) is the condition of incompressibility, and (2.2) is a diffusion–advection equation, with diffusion coefficient D_ϕ . Equation (2.4) is the Poisson equation, with ψ the electrostatic potential, e the electron's charge, and ε_0 and $\varepsilon(\phi)$ the vacuum and relative permittivities, respectively. Equation (2.5) is the Poisson–Nernst–Planck equation, with ion diffusion constant D_i common to both ionic species. We use a modified Poisson–Boltzmann framework that takes the finite volume of the ions into account, thus

$$\phi + \phi_{cs} + v_0 n^+ + v_0 n^- = 1, \tag{2.6}$$

where v_0 is a volume common to all molecules – water, cosolvent and ions. Equation (2.3) is a Navier–Stokes equation with a force due to composition gradients, and a term \mathbf{f}_{elec} , derivable from the Maxwell stress tensor, given by $\mathbf{f}_{elec} = (1/2) \nabla (\varepsilon_0 E^2 \phi \partial \varepsilon / \partial \phi)_T - (1/2) \varepsilon_0 E^2 \nabla \varepsilon + e(n^+ - n^-) \mathbf{E}$, with the electric field $\mathbf{E} = -\nabla \psi$. The composition-dependent permittivity is taken to be

$$\varepsilon(\phi) = \varepsilon_{cs} \phi_{cs} + \varepsilon_w (1 - \phi_{cs}), \tag{2.7}$$

where ε_w and ε_{cs} are the water and cosolvent permittivities, respectively.

The dependence of viscosity on composition is essential for electrolubrication. We assume that the ions' contribution to the viscosity is the same as that of water, and use the following linear constitutive relation:

$$\eta(\phi) = \eta_{cs} \phi_{cs} + \eta_w (1 - \phi_{cs}). \tag{2.8}$$

The assumption of an infinitely long channel means that the flow velocity is parallel to the channel axis: $\mathbf{v} = v(x) \hat{y}$. In steady state, all time derivatives vanish. Since there is no flux of mixture or ions from the walls, we arrive at a remarkable simplification to (2.1)–(2.5) – both the composition profile $\phi(x)$ and ionic densities extremize the free energy: $\delta f / \delta \phi = 0$ and $\delta f / \delta n^\pm = 0$. As in equilibrium, they do not depend on D_ϕ and D_i .

Once $\phi(x)$ and $n^\pm(x)$ are found, one needs to solve the Navier–Stokes equation

$$0 = -\partial_y p_0 + \partial_x (\eta(\phi(x)) \partial_x v(x)) \quad (2.9)$$

subject to the two boundary conditions $v(x = \pm D/2) = 0$.

2.1. Free energy

To be specific, we use below the free energy model

$$\left. \begin{aligned} \Omega &= \int_{-D/2}^{D/2} (f - \lambda^+ n^+ - \lambda^- n^- - \mu \phi / v_0) dx + f_s, \\ f &= \frac{1}{2} c^2 (\nabla \phi)^2 + f_m + f_e + f_i. \end{aligned} \right\} \quad (2.10)$$

The channel walls are taken to be symmetric, hence the surface energy f_s is taken as $f_s = \Delta\gamma(\phi(-D/2) + \phi(D/2))$, where $\Delta\gamma$ is the difference between the surface energies of water and cosolvent. The chemical potentials of the cations and anions are λ^\pm , respectively, and that of the mixture is μ . The square-gradient term accounts for the energetic cost of composition inhomogeneities, where c is a constant.

The free energy density of mixing is

$$f_m = \frac{k_B T}{v_0} [\phi \log(\phi) + \phi_{cs} \log(\phi_{cs}) + \chi \phi \phi_{cs}], \quad (2.11)$$

where k_B is the Boltzmann constant, T is the absolute temperature, and $\chi \sim 1/T$ is the Flory interaction parameter. Equation (2.11) leads to an upper critical solution temperature type phase diagram. In the ϕ – χ plane, a homogeneous phase is stable above the binodal curve $\phi_b(\chi)$, whereas below it, the mixture separates to water-rich and water-poor phases, with compositions given by $\phi_b(\chi)$. The two phases become indistinguishable at the critical point $(\phi_c, \chi_c) = (1/2, 2)$.

The electrostatic energy density f_e is given by

$$f_e = -\frac{1}{2} \varepsilon_0 \varepsilon(\phi) (\nabla \psi)^2 + e(n^+ - n^-) \psi. \quad (2.12)$$

The free energy density of the ions, f_i , is modelled as

$$f_i = k_B T [\ln^+(v_0 n^+) - 1) + n^- (\ln(v_0 n^-) - 1) - \phi(\Delta u^+ n^+ + \Delta u^- n^-)]. \quad (2.13)$$

The logarithmic terms account for the ions' entropy; the terms proportional to ϕ model specific chemical short-range interactions between ions and solvents. The parameters Δu^\pm measure the preference of ions towards a water environment and are of order ~ 1 – 10 (Marcus 1988; Samin & Tsori 2012, 2013). In the following, we deal with ions that are preferentially hydrophilic, and take them as equal: $\Delta u^\pm = \Delta u$.

2.2. Free energy minimization

We use the following dimensionless variables: $\tilde{x} = x/\lambda_D$, $\lambda_D^2 = \varepsilon_0 \varepsilon(\phi_0) k_B T / (2n_0 e^2)$, $\tilde{\psi} = e\psi/k_B T$, $\tilde{V} = eV/k_B T$, $\tilde{n}^\pm = v_0 n^\pm$, $\tilde{n}_0 = v_0 n_0$, $\tilde{c}^2 = c^2 v_0 / (\lambda_D^2 k_B T)$, $\tilde{\mu} = \mu/k_B T$, $\tilde{f}_m = v_0 f_m/k_B T$ and $\Delta \tilde{\gamma} = \Delta\gamma \lambda_D / c^2$. Here, n_0 and ϕ_0 are the bulk ion density and mixture composition, respectively, λ_D is the Debye length, and V is the potential drop across the

channel. Using these definitions, one can extremize the energy to find the profiles $\phi(x)$ and $\psi(x)$ as

$$-\tilde{c}^2 \tilde{\nabla}^2 \phi + \frac{\partial \tilde{f}_m}{\partial \phi} - \Delta u^+ \tilde{n}^+ - \Delta u^- \tilde{n}^- - \frac{1}{2} \frac{2\tilde{n}_0}{\varepsilon(\phi_0)} \frac{\partial \varepsilon}{\partial \phi} (\tilde{\nabla} \tilde{\psi})^2 - \tilde{\mu} = 0, \quad (2.14)$$

$$\tilde{\nabla} \cdot (\varepsilon(\phi) \tilde{\nabla} \tilde{\psi}) = \frac{\varepsilon(\phi_0)}{2\tilde{n}_0} (\tilde{n}^- - \tilde{n}^+). \quad (2.15)$$

The first equation expresses the variation with respect to ϕ , i.e. $\delta f/\delta \phi = 0$, and the second equation is Poisson's equation. The boundary conditions for ϕ and $\tilde{\psi}$ are

$$\left. \begin{aligned} \phi'(\tilde{x} = \pm \tilde{D}/2) &= \mp \frac{\Delta \tilde{\gamma}}{\tilde{c}^2}, \\ \tilde{\psi}(\tilde{x} = \pm \tilde{D}/2) &= \pm \frac{1}{2} \tilde{V}. \end{aligned} \right\} \quad (2.16)$$

The ions obey a modified Boltzmann distribution (Borukhov, Andelman & Orland 1997; Samin & Tsori 2016):

$$\left. \begin{aligned} \tilde{n}^\pm &= \frac{P^\pm (1 - \phi)}{1 + P^+ + P^-}, \\ P^\pm &= \frac{\tilde{n}_0}{1 - \phi_0 - 2\tilde{n}_0} \exp \left[(\phi - \phi_0)(\chi + \Delta u^\pm) \mp \tilde{\psi} \right]. \end{aligned} \right\} \quad (2.17)$$

In general, the electric double layer created at the walls leads to adsorption of the polar solvent due to the dielectrophoretic force and preferential solvation. The thickness of the resulting lubrication layer is determined by both the Debye length and the correlation length of the mixture ξ , and thus can be large at temperatures close to the critical point (Tsori & Leibler 2007; Samin & Tsori 2013).

2.3. Velocity profile

Once the the composition profile $\phi(x)$ is known from (2.14), (2.15) and (2.17), $v(x)$ can be found in the following way from (2.9). We write the constant pressure drop along the channel as $-\partial_y p_0 \equiv -\Delta p/L$, where Δp is the pressure drop over a channel of length L . Using the symmetry of the problem with respect to the reflection $x \rightarrow -x$, one arrives at the solution for the flow profile $v(x)$ given by

$$v_{ef}(x) = \frac{\Delta p}{L} \int_{-D/2}^x \frac{x'}{\eta(\phi(x'))} dx'. \quad (2.18)$$

The no-flow condition at the walls, $v(x = \pm D/2) = 0$, is satisfied. The total flux is given by the integral

$$Q_{ef} = \int_{-D/2}^{D/2} v(x) dx. \quad (2.19)$$

Recall that when the mixture is homogeneous with composition ϕ_0 and viscosity $\eta_0 = \eta(\phi_0)$, $v(x)$ is the classical parabolic profile

$$v_m(x) = \frac{1}{2} \frac{\Delta p}{\eta_0 L} \left(x^2 - \left(\frac{D}{2} \right)^2 \right). \quad (2.20)$$

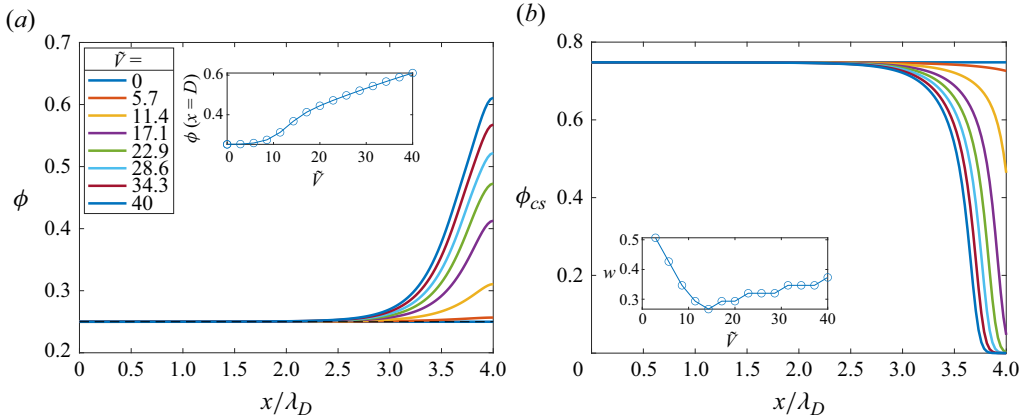


Figure 2. (a) Water (ϕ) profiles for varying values of scaled potential \tilde{V} (see legend). The total channel width is $D = 8\lambda_D$, and the walls are located at $x/\lambda_D = \pm 4$. The inset shows the surface value $\phi(x = D)$ versus \tilde{V} . (b) Cosolvent (ϕ_{cs}) profiles for the same potentials. The inset is the width of the wetting layer close to the wall w , defined as the distance from the walls, where ϕ is the average between ϕ_0 and $\phi(x = D)$. In all figures, unless stated otherwise, we used $\phi_0 = 0.25$, $\chi = 1$, $\Delta u = 2$, $\varepsilon_w = 80$, $\varepsilon_{cs} = 45$, $\tilde{c} = 0.4$, $\eta_{cs}/\eta_w = 1412$, $\Delta\tilde{\gamma} = 0$ and $\tilde{\eta}_0 = 0.001$.

The flux of this mixed state is

$$Q_m = -\frac{1}{12} \frac{\Delta p}{\eta_0 L} D^3. \tag{2.21}$$

The ‘flow amplification factor’ α is defined as the ratio between the fluxes with and without electrostatic potential:

$$\alpha = \frac{Q_{ef}}{Q_m}, \tag{2.22}$$

with the integrated fluxes Q_{ef} and Q_m taken from (2.19) and (2.21), respectively.

In the next section we solve numerically the profiles $\phi(x)$ and $\psi(x)$, evaluate the velocity and flux from (2.18) and (2.19) for the state with an electric field, and compare them with the same quantities without the field.

3. Results

We solve (2.14) and (2.15) numerically as diffusion equations with pseudo-time until the solutions do not change within the desired error. Spatial derivatives were discretized using standard schemes, and the time integration was done using the Runge–Kutta algorithm. The results were substituted in the equations to verify their validity. For example, in (2.15), the right- and left-hand sides were verified to be equal within a relative error of 10^{-3} . We used channels with scaled width $D = 8\lambda_D$ and several values of cross-channel potential \tilde{V} .

Figure 2(a) shows the water composition, and figure 2(b) the cosolvent composition, across the channel as a function of increasing potential. When $\tilde{V} = 0$, ϕ equals the bulk composition $\phi_0 = 0.25$. As \tilde{V} increases, two boundary layers appear at the walls. The value of ϕ increases near the walls, while ϕ_{cs} decreases. Their sum is not exactly unity since the dissolved ions have finite volumes. Note that $\tilde{V} = 40$ corresponds to a physical potential of 1 V. Clearly, at the walls, water is enriched, therefore the viscosity there is greatly reduced locally as compared to the centre of the channel ($x = 0$). The inset in

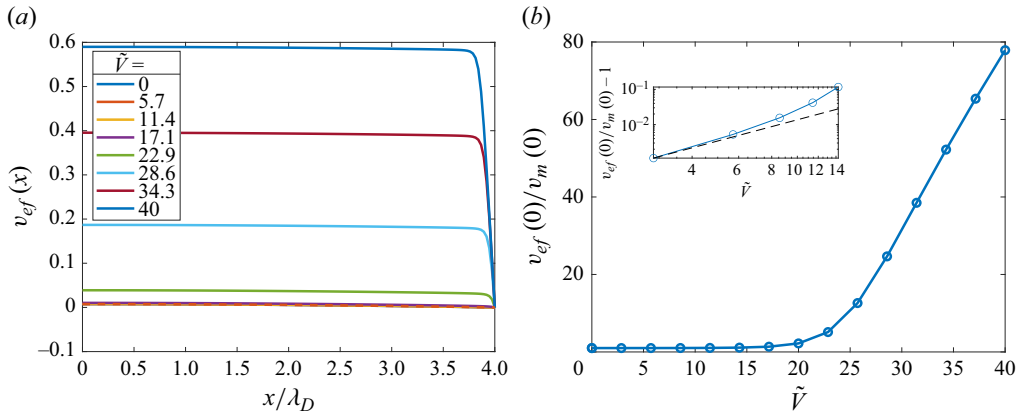


Figure 3. (a) Velocity profile $v(x)$ across the channel from (2.18) for varying values of scaled potential \tilde{V} (see legend). When $\tilde{V} = 0$, the mixture is homogeneous. The flow is then parabolic and given by (2.20). It is not visible because its amplitude is too small. Here, v_{ef} is given in units of $\Delta p \lambda_D^2 / (L \eta_w)$. (b) The ratio of the mid-channel velocities with and without electric potential, $v_{ef}(0)/v_m(0)$, for varying potentials. The inset is a log–log plot indicating that $v_{ef}(0)/v_m(0) - 1 \sim \tilde{V}^2$ (slope of dashed line is 2).

figure 2(b) shows the width of the water layer near the walls, w , which depends on the electrostatic screening length and on the mixture’s correlation length. The non-monotonic behaviour of w versus \tilde{V} is a result of the simultaneous nonlinear decrease of screening and the stronger adsorption of water with increasing \tilde{V} .

Figure 3(a) shows the resultant velocity profiles $v_{ef}(x)$ calculated from (2.18) for the same values of \tilde{V} . The curves are characterized by a thin boundary layer at the walls, where the gradient of $v_{ef}(x)$ is large, and a large region, far from the walls, where the velocity is high and approximately constant. As \tilde{V} increases, the maximal speed in the centre increases, and the gradient v'_{ef} near the walls becomes even larger. Using the numerical values $\Delta p = 1$ atm, $L = 0.01$ m and $\lambda_D = 10$ nm, we estimate v_{ef} to be of the order of $1 \mu\text{m s}^{-1}$ for the largest potential, $\tilde{V} = 40$. This is almost 80 times larger than the velocity in the absence of potential.

In figure 3(b), we plot the ratio of the velocities with and without a field, v_{ef}/v_m . Both are evaluated at their maximum, i.e. at $x = 0$, and $v_m(x)$ is the parabolic profile in (2.20). When $\tilde{V} = 0$, the two are equal. The ratio increases with \tilde{V} to high values – at a physical potential of just 1 V, $v_{ef}(0)/v_m(0)$ is near 80.

In the calculations thus far, the walls were neither hydrophilic nor hydrophobic, $\Delta\tilde{\gamma} = 0$. It is interesting to study how the flow is affected by the relative hydrophilicity of the surfaces by allowing $\Delta\tilde{\gamma}$ to vary. Figure 4 shows the ‘flow amplification factor’ α from (2.22). As expected, the general trend is that $\alpha(\tilde{V})$ increases with \tilde{V} . Each curve corresponds to a different value of $\Delta\tilde{\gamma}$. While all curves reach large flow amplification at $\tilde{V} = 40$ ($\alpha \sim 100$ for all curves), it is clear that α becomes larger monotonically as the surface hydrophilicity increases.

In figure 5, we look at the dependence of electrolubrication on the salt content. We calculated Q_{ef} versus \tilde{V} with a given amount of salt \tilde{n}_0 , and then repeated with more salt. While α increases with \tilde{V} and reaches high values at $\tilde{V} = 40$, it also increases monotonically as salt is added.

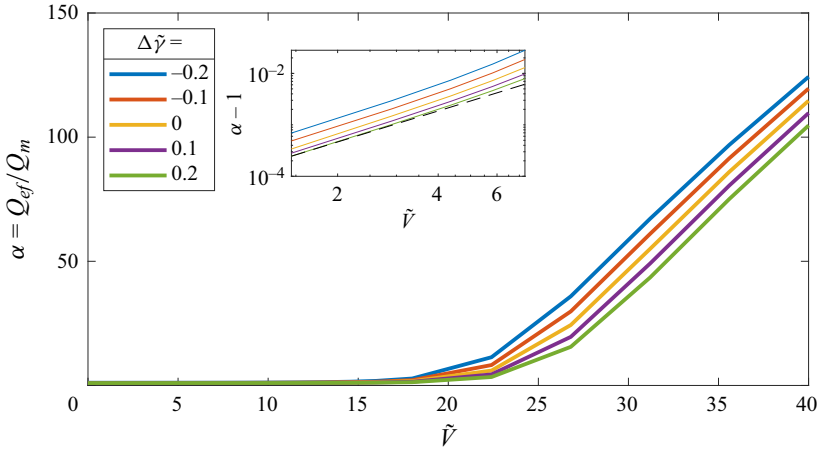


Figure 4. Flow amplification factor α versus \tilde{V} for different values of $\Delta\tilde{\gamma}$. Here, α in (2.22) is defined as the ratio of the total channel flux with and without electric potential, with Q_{ef} and Q_m taken from (2.19) and (2.21), and Q_m is the flux of the classical parabolic profile, in the absence of potential. The curves differ by the value of $\Delta\tilde{\gamma}$ (see legend). As the walls become more hydrophilic (decreasing value of $\Delta\tilde{\gamma}$), the flux increases relative to Q_m . The inset is a log–log plot indicating that $\alpha - 1 \sim \tilde{V}^2$ (slope of dashed line is 2).

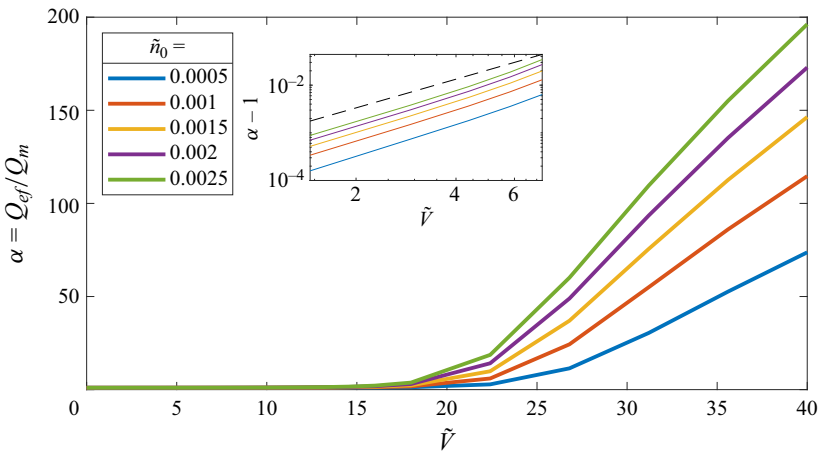


Figure 5. Flow amplification factor α versus \tilde{V} for different salt contents; the legend indicates the value of \tilde{n}_0 . As salt is added, the walls adsorb more water, and the flux increases relative to Q_m , with $\Delta\tilde{\gamma} = 0$. In all curves, $D = 8\lambda_D$, with λ_D depending on \tilde{n}_0 . The inset is a log–log plot indicating that $\alpha - 1 \sim \tilde{V}^2$ (slope of dashed line is 2).

Until now, the polar liquid (water) was considered to be less viscous than the non-polar one (cosolvent), thereby facilitating the two lubrication layers when potential is applied across the walls. It is tempting to think of the opposite case, where the polar liquid is more viscous. If this liquid is very viscous, then could the two layers at the walls act as ‘pipe cloggers’, effectively reducing the channel width D (or pipe diameter in the case of a circular pipe)?

Figure 6 examines this situation. All parameter values are the same as in figures 2 and 3, except that the viscosities are interchanged: $\eta_w/\eta_{cs} = 1412$. In figure 6(a), v_{ef} is shown for varying values of \tilde{V} . The flow velocity is slower at any point x , and, in particular, in

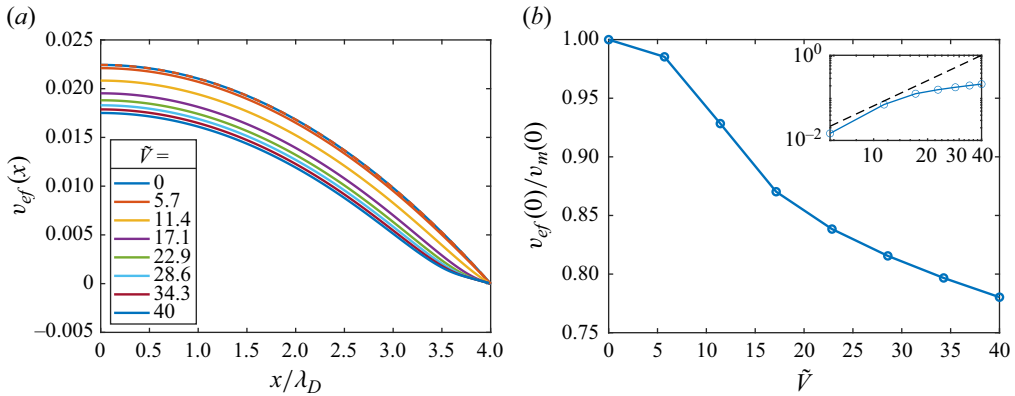


Figure 6. The same as in figure 3, but now the polar liquid is the more viscous one, i.e. assuming $\eta_w/\eta_{cs} = 1412$. The dashed line in panel (a) is the classical parabolic profile $v_m(x)$. The limit $\tilde{V} \rightarrow \infty$ describes complete separation between the liquids, where their velocities given by (3.1). When $\eta_w \gg \eta_{cs}$, and using $\phi_0 = 2w/D$, one finds that the curve in panel (b) tends to $v_{ef}(0)/v_m(0) \approx (1 - \phi_0)^2 = 0.56$ in the large potential limit when $\phi_0 = 0.25$. The inset is a log–log plot of $1 - v_{ef}(0)/v_m(0)$ versus \tilde{V} . The slope of the dashed line is 2.

the centre. Figure 6(b) quantifies the reduction of the flow velocity in the centre. At the maximum value, $\tilde{V} = 40$, the velocity is reduced by a modest $\sim 25\%$ from its no-field case. The inset shows that $1 - v_{ef}(0)/v_m(0) \sim \tilde{V}^2$.

The figures above show a dependence on \tilde{V}^2 for small potentials. The small \tilde{V} limit can be obtained as follows: (2.14) is linearized around the bulk composition ϕ_0 using the Debye–Hückel solution of (2.15). The homogeneous solution includes exponents with the mixture correlation length, and the particular solution includes the Debye length. Next, the Navier–Stokes equation (2.9) is solved by assuming that $v(x) = v_0(x) + \delta v(x)$, where v_0 is the parabolic profile, and δv is a small perturbation whose boundary values are $\delta v(x = \pm D/2) = 0$. The dependence of δv on ϕ is via (2.8). The perturbation δv and the corresponding flux are proportional to \tilde{V}^2 . As a result, $1 - v_{ef}(0)/v_m(0) \sim \tilde{V}^2$.

How does α scale with the channel width D ? In figure 7, we varied D at constant pressure gradient and potential. Figure 7(a) shows the profiles $\phi(x)$ versus x for several values of D (different colours; see legend). Note that each curve has a different x -range. All curves exhibit a wetting layer near the walls. These layers are similar to each other because the potential is the same. The calculations assume that far from the surfaces, the composition is fixed at $\phi_0 = 0.25$. Figure 7(b) shows α versus D . At small channel widths, α is large since the volume fraction of the less viscous solvent (water) is high. As D increases, the volume fraction of the wetting layers becomes smaller, and α decreases monotonically. In the limit $D \rightarrow \infty$, α tends to unity.

We now estimate α by using a simple analytical model, where two layers of pure water of thickness w are at the walls, and pure cosolvent is in the centre. Hence $\phi_0 = 2w/D$ is the water volume fraction. From (2.18), one finds the velocity in the two regions to be

$$\left. \begin{aligned} v_{cs}(x) &= \frac{1}{2} \frac{\Delta p}{\eta_{cs} L} x^2 + c_1, & |x| \leq D/2 - w, \\ v_w(x) &= \frac{1}{2} \frac{\Delta p}{\eta_w L} x^2 + c_2, & |x| > D/2 - w. \end{aligned} \right\} \quad (3.1)$$

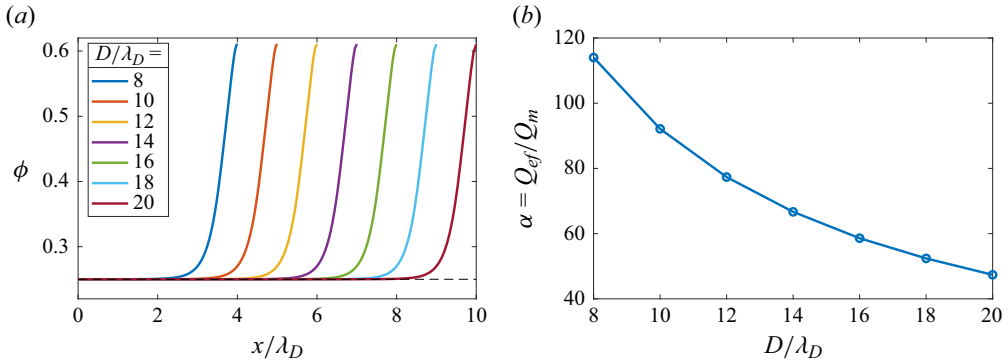


Figure 7. (a) Composition profiles for different channel widths D (see legend) at constant potential $\tilde{V} = 40$. Each curve has a different x -range: for example, the dark blue curve corresponds to $D = 8\lambda_D$, therefore the x -range is $-4 \leq x/\lambda_D \leq 4$. All curves have a wetting layer of the less viscous liquid at $x \lesssim D$. Calculations assume a bulk value $\phi_0 = 0.25$ far from the walls. (b) Flow amplification ratio α versus channel width D . Here, α decreases with D since the relative volume fractions of the wetting layers decreases with D .

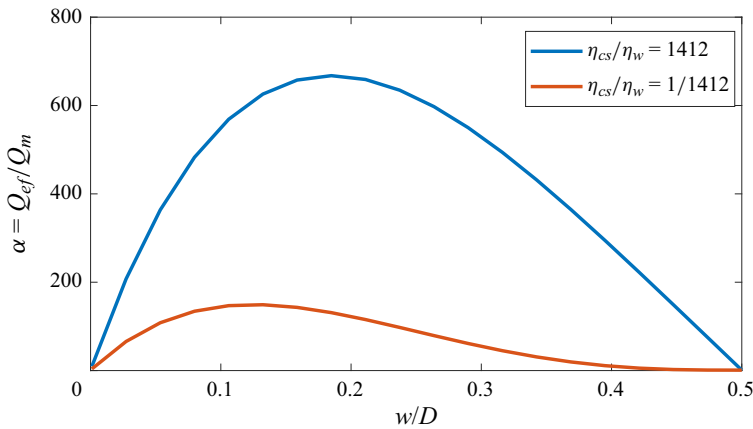


Figure 8. Flow amplification factor α as a function of model layer thickness w . This layer comprises the more polar liquid, and its viscosity is η_w . The viscosity of the non-polar liquid in the centre of the channel is η_{cs} . The blue curve is where the polar layer is less viscous; the red curve is where the polar layer is more viscous.

From the continuity of v at $x = \pm(D/2 - w)$, and the no-flow boundary conditions, it follows that $c_2 = (-1/8) \Delta p D^2 / (\eta_w L)$ and $c_1 = (\Delta p / 2L) (1/\eta_w - 1/\eta_{cs}) (D/2 - w)^2 - (1/8) \Delta p D^2 / (\eta_w L)$.

The flux integrated over the channel width is

$$\begin{aligned}
 Q_{ef} &= 2 \int_0^{D/2-w} v_{cs} dx + 2 \int_{D/2-w}^{D/2} v_w dx \\
 &= -\frac{1}{12} \frac{\Delta p}{L} \frac{2w(3D^2 - 6Dw + 4w^2) \eta_{cs} + (D - 2w)^3 \eta_w}{\eta_{cs} \eta_w}.
 \end{aligned} \tag{3.2}$$

The flux of the mixed state can be obtained from (2.21), with the average viscosity given by $\eta_0 = (2w/D)\eta_w + (1 - 2w/D)\eta_{cs}$:

$$Q_m = -\frac{1}{12} \frac{\Delta p}{L} \frac{D^3}{\frac{2w}{D} \eta_w + \left(1 - \frac{2w}{D}\right) \eta_{cs}}. \quad (3.3)$$

The ratio $\alpha = Q_{ef}/Q_m$ increases monotonically with the viscosity ratio η_{cs}/η_w when w/D is held constant. One can also hold the ratio η_{cs}/η_w constant and inspect α as a function of w/D . The small w/D values correspond to the large D range in figure 7(b). Surprisingly, as can be seen in figure 8, α has a maximum at a finite lubrication layer thickness w . The blue curve shows α for the case where the less polar liquid is more viscous ($\eta_{cs}/\eta_w = 1412$). In the red curve, the viscosities are interchanged: the polar phase is more viscous, $\eta_w/\eta_{cs} = 1412$. The existence of the maximum is due to the assumption of a closed system, where η_0 depends on w , D , η_{cs} and η_w , which is different from a system coupled to a reservoir, where $\eta_0 = \eta_{cs}$.

4. Conclusion

We investigate the electrolubrication of liquid mixtures flowing between two parallel plates. An electrostatic potential applied across the surfaces causes partial demixing of the liquids. The more polar liquid is adsorbed to the walls, due to screening of dissolved ions. The thickness of the lubrication layer can be large at temperatures close to the critical point. A similar phenomenon could be achieved, in principle, without ionic screening, but the geometry would have to allow for field gradients (Tsori, Tournilhac & Leibler 2004). In addition, the potentials required are higher.

When the more polar liquid is less viscous than the non-polar one, shear stress falls mainly on the thin lubrication layers, and the flow profile is modified significantly from the classical parabolic one. The velocity and flux in the gap are then increased. The ‘flow amplification factor’ α , measuring the relative increase in flux, is of order 10–100 or more for mixtures of water and glycerol. It increases monotonically with applied potential. Additionally, α depends on the viscosity ratio, ionic content, temperature and surface tension with the walls.

The flow profile in figure 1(b) is reminiscent of yield stress phenomena in Bingham fluids. Usually in yield stress phenomena, the fluid is homogeneous, and the yielding occurs when the pressure is larger than a critical value. Here, the fluid is made up from two liquids, and ‘yielding’ is due to the field acting transverse to the flow while the pressure is constant.

One possible application of ‘electrolubrication’ is in microfluidic devices, whereby the flow of liquid mixtures flowing in narrow channels could be manipulated by transverse potentials. Electrical contacts are already commonly used to control the location and movement of droplets transport in channels. As we show in this paper, precise temperature regulation or exact solution composition are not required. Another possible application is in microelectromechanical systems, where small, solid, moving elements slide past each other. If the liquid embedding the moving parts is a mixture, then control of the elements’ charge would allow us to modify the lubrication layer around the elements, and therefore the friction. In many cases, solid surfaces are charged (e.g. silica in aqueous water), and then it is important to assess the lubrication effect.

It would be interesting to lift the assumption of steady state and study, for example, a homogeneous mixture entering a constriction subject to strong electric field. The mixture’s

composition and velocity then evolve along the flow direction, and reach steady state only sufficiently far downstream. The understanding of such dynamical processes is not trivial and could be important for various applications of electrolubrication.

Funding. This work was supported by the Israel Science Foundation (ISF) grant no. 274/19.

Declaration of interests. The authors report no conflict of interest.

Author ORCID.

 Roni Kroll <https://orcid.org/0000-0002-3448-0642>;

 Yoav Tsori <https://orcid.org/0000-0003-3664-6498>.

REFERENCES

- ANDRADE, E.N. DA C. & DODD, C. 1939 Effect of an electric field on the viscosity of liquids. *Nature* **144** (3637), 117–118.
- ANDRADE, E.N. DA C. & DODD, C. 1946 The effect of an electric field on the viscosity of liquids. *Proc. R. Soc. Lond. A* **187** (1010), 296–337.
- BORUKHOV, I., ANDELMAN, D. & ORLAND, H. 1997 Steric effects in electrolytes: a modified Poisson–Boltzmann equation. *Phys. Rev. Lett.* **79** (3), 435.
- BRESME, F., KORNYSHEV, A.A., PERKIN, S. & URBACH, M. 2022 Electrotunable friction with ionic liquid lubricants. *Nat. Mater.* **21** (8), 848–858.
- FAJARDO, O.Y., BRESME, F., KORNYSHEV, A.A. & URBACH, M. 2017 Water in ionic liquid lubricants: friend and foe. *ACS Nano* **11** (7), 6825–6831.
- GROPPER, D., WANG, L. & HARVEY, T.J. 2016 Hydrodynamic lubrication of textured surfaces: a review of modeling techniques and key findings. *Tribol. Intl* **94**, 509–529.
- HAO, T. 2001 Electrorheological fluids. *Adv. Mater.* **13** (24), 1847–1857.
- HU, Y.-Z. & GRANICK, S. 1998 Microscopic study of thin film lubrication and its contributions to macroscopic tribology. *Tribol. Lett.* **5**, 81–88.
- KLEIN, J. 1996 Shear, friction, and lubrication forces between polymer-bearing surfaces. *Annu. Rev. Mater. Sci.* **26** (1), 581–612.
- LUGT, P.M. 2009 A review on grease lubrication in rolling bearings. *Tribol. Trans.* **52** (4), 470–480.
- MARCUS, Y. 1988 Preferential solvation of ions in mixed solvents. Part 2. The solvent composition near the ion. *J. Chem. Soc. Faraday Trans.* **84** (5), 1465–1473.
- MARSH, K.N., BOXALL, J.A. & LICHTENTHALER, R. 2004 Room temperature ionic liquids and their mixtures – a review. *Fluid Phase Equilib.* **219** (1), 93–98.
- PIVNIC, K., BRESME, F., KORNYSHEV, A.A. & URBACH, M. 2020 Electrotunable friction in diluted room temperature ionic liquids: implications for nanotribology. *ACS Appl. Nano Mater.* **3** (11), 10708–10719.
- PIVNIC, K., DE SOUZA, J.P., KORNYSHEV, A.A., URBACH, M. & BAZANT, M.Z. 2023 Orientational ordering in nano-confined polar liquids. *Nano Lett.* **23** (12), 5548–5554.
- SAMIN, S. & VAN ROIJ, R. 2017 Interplay between adsorption and hydrodynamics in nanochannels: towards tunable membranes. *Phys. Rev. Lett.* **118** (1), 014502.
- SAMIN, S. & TSORI, Y. 2012 The interaction between colloids in polar mixtures above t_c . *J. Chem. Phys.* **136** (15), 154908.
- SAMIN, S. & TSORI, Y. 2013 Stabilization of charged and neutral colloids in salty mixtures. *J. Chem. Phys.* **139** (24), 244905.
- SAMIN, S. & TSORI, Y. 2016 Reversible pore gating in aqueous mixtures via external potential. *Colloid Interface Sci. Commun.* **12**, 9–12.
- SWEENEY, J., HAUSEN, F., HAYES, R., WEBBER, G.B., ENDRES, F., RUTLAND, M.W., BENNEWITZ, R. & ATKIN, R. 2012 Control of nanoscale friction on gold in an ionic liquid by a potential-dependent ionic lubricant layer. *Phys. Rev. Lett.* **109** (15), 155502.
- TERWAGNE, D., BROJAN, M. & REIS, P.M. 2014 Smart morphable surfaces for aerodynamic drag control. *Adv. Mater.* **26** (38), 6608–6611.
- TSORI, Y. 2023 Electrolubrication in flowing liquid mixtures. *Phys. Fluids* **35** (7), 073306.
- TSORI, Y. & LEIBLER, L. 2007 Phase-separation in ion-containing mixtures in electric fields. *Proc. Natl Acad. Sci. USA* **104** (18), 7348–7350.
- TSORI, Y., TOURNILHAC, F. & LEIBLER, L. 2004 Demixing in simple fluids induced by electric field gradients. *Nature* **430** (6999), 544–547.